Structures 6 (2016) 134–145

Contents lists available at ScienceDirect

Structures

journal homepage: www.elsevier.com/locate/structures

# Finite element modeling of structural steel component failure at elevated temperatures

Mina Seif *, Joseph Main, Jonathan Weigand, Therese P. McAllister, William Luecke

*National Institute of Standards and Technology (NIST), 100 Bureau Drive, Stop 8611, Gaithersburg, MD 20899, USA*

ARTICLE INFO

*Article history:*
Received 22 October 2015
Received in revised form 9 March 2016
Accepted 11 March 2016
Available online 12 March 2016

*Keywords:*
Stress–strain relationship
Fire loading
Uniform strain
Elevated temperatures
Finite element
Fracture

ABSTRACT

A key issue in evaluating the response of structural systems to fire effects is the representation of material behavior at elevated temperatures. In addition to stress–strain behavior, modeling of fracture is required to capture failure modes such as tear out in connection plates and bolt shear. Fracture can be simulated in explicit finite element analysis using element erosion, in which elements are removed from the analysis when specified failure criteria are satisfied. However, the basis for determining and implementing material failure criteria at elevated temperatures is not well-established in the literature. A finite element material modeling methodology is presented for structural steels and structural bolts at elevated temperatures that incorporates erosion-based modeling of fracture. Temperature-dependent stress–strain relationships for structural steel and structural bolts were combined with a plastic strain-based failure criterion for element erosion to enable modeling of fracture in analysis of structural connections and assemblies. The failure criterion was calibrated against high-temperature experimental data on elongation of tensile coupons at fracture, and its dependence on temperature and mesh size was investigated.



## 1. Introduction

Fire effects on steel structures can produce failures of connections, including fracture of connection plates, shear rupture of bolts, and bolt tear-out failure of beam webs or connection plates. Fig. 1 illustrates such failure modes for a typical shear tab connection at elevated temperatures, based on explicit finite element analyses described by Seif et al. [1]. Whether such failures occur depends not only on the loads that can be sustained by the various components of a connection, but also on the deformations that can be accommodated prior to fracture, since fire-induced forces result from the restraint of thermal expansion or contraction. The ductility of steel components thus plays an important role in the performance of connections at elevated temperatures. In addition, ductility can potentially allow redistribution of loads after failure of one or more connection components.

While implicit finite element methods are prone to convergence problems when local failures occur, explicit finite element methods are well suited for simulating successive failures and the subsequent redistribution of loads. Fracture for both tensile and shear failure modes can be simulated in explicit analyses (in an approximate sense) using element erosion, in which elements are automatically removed from the analysis when specified failure criteria are met. The erosion process may continue until a component has lost elements across its entire section, representing complete fracture, as illustrated in Fig. 1(c). The basis for determining and implementing material failure criteria at elevated temperatures, however, is not well-established in the literature. The objective of this paper is to demonstrate a practical material modeling approach for structural steel and structural bolts at elevated temperatures that incorporates erosion-based modeling of fracture and that can be implemented in FE analysis using currently available tensile coupon data at elevated temperatures. Such an approach is needed in the context of performance-based design, to enable evaluation of the performance structural components, assemblies, and systems under fire effects.

Failure modes such as tear-out and bolt shear rupture are ductile fractures with significant plastic deformation before fracture, particularly at elevated temperatures. Key factors influencing the initiation of ductile fracture in steel are the equivalent plastic strain and the stress triaxiality, defined as the ratio of the mean or hydrostatic stress to the effective or von Mises stress. Micromechanics-based models for predicting ductile fracture generally require calibration against experimental fracture data at different levels of triaxiality (e.g., Kanvinde and Deierlein [2]). However, experimental data on fracture of steel at elevated temperatures are currently insufficient to enable calibration of such micromechanics-based models. Accordingly, researchers tend to model strain hardening and softening, but do not address fracture at elevated temperatures (e.g. Garlock and Selamet [3], Sarraj et al. [4], and Pakala et al. [5]). The material model for structural steel at elevated temperatures in the Eurocode [6] also does not address material

* Corresponding author.
*E-mail addresses:* mina.seif@nist.gov (M. Seif), joseph.main@nist.gov (J. Main), jonathan.weigand@nist.gov (J. Weigand), therese.mcallister@nist.gov (T.P. McAllister), william.luecke@nist.gov (W. Luecke).

http://dx.doi.org/10.1016/j.istruc.2016.03.002
2352-0124/

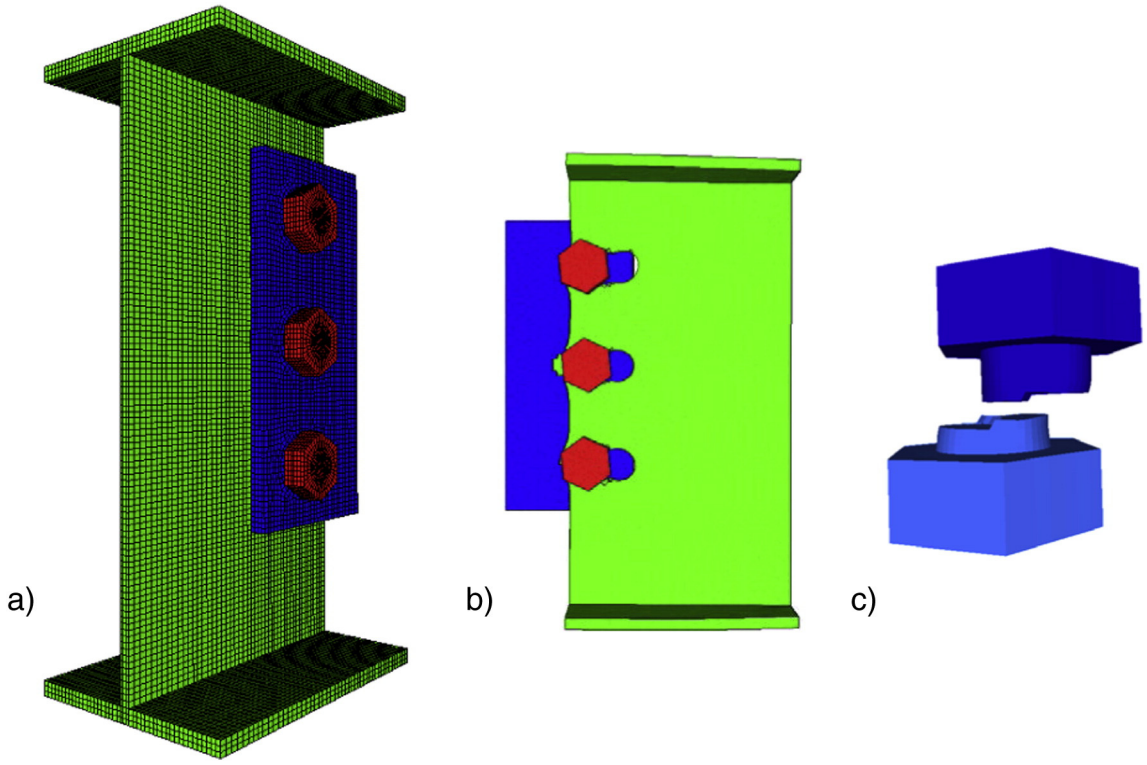


**Fig. 1.** (a) Detailed model of a shear tab connection, (b) tear-out failure in beam web, and (c) shear fracture of a bolt.

fracture. Instead, the yield strength is reduced to zero with a linear material softening between 15% and 20% strain.

The proposed material modeling approach for structural steel uses an empirical power–law form of stress–strain relationship recently developed by Luecke (Seif et al. [7]), which was fit to a large set of experimental data at elevated temperatures. A tri-linear stress–strain relationship is proposed to model the temperature-dependent behavior of structural bolts, for which experimental data at elevated temperatures are more limited. Rather than using a micromechanics-based model, a relatively simple plastic strain-based failure criterion is proposed for modeling fracture of both structural steel and structural bolts in structural system analyses. Similar approaches have been successfully implemented in detailed finite element analyses of moment connections (Sadek et al. [8]) and simple shear connections (Main and Sadek [9]) under column removal scenarios at ambient temperature. In this study, the erosion strain (the local plastic strain at which element erosion is activated) was calibrated against available high-temperature experimental data on elongation of tensile coupons at fracture, and it was found that a temperature-dependent value of the erosion strain was required to capture the experimental data. The dependence of the failure criterion on temperature and mesh size was also investigated, and for structural bolts, analyses of double-shear tests were performed to assess the performance of the material modeling approach under shear loading.

## 2. Temperature-dependent material model for structural steel

The material model developed by Luecke (Seif et al. [7]) is a temperature-dependent empirical model for any structural steel with a nominal yield strength less than 450 MPa (65 ksi). The model is based on experiments conducted at the National Institute of Standards and Technology (NIST) and experimental data gathered from multiple sources reported in the literature. The model accounts for temperature-dependent changes in yield strength and post-yield strain hardening but does not include creep effects. The model, presented in Section 2.1, is formulated in terms of true stress as a function of true strain, as is typical in material models for continuum finite element analysis. Relationships between true stress–strain and engineering stress–strain for uniaxial tension are presented subsequently in Section 2.2, which discusses the onset of necking at the ultimate tensile strength. Section 2.3 discusses the modeling of post-ultimate necking behavior and erosion-based modeling of fracture. Finally, Section 2.4 addresses some of the assumptions and limitations associated with this modeling approach.

### 2.1. True stress–strain relationship

The temperature-dependent relationship between true stress and true strain incorporates temperature-dependent expressions for the elastic modulus and the yield strength. The elastic modulus $E$ is expressed as follows:

$$E(T) = E_0\left[\exp\left(-\frac{1}{2}\left(\frac{\Delta T}{e_3}\right)^{e_1} - \frac{1}{2}\left(\frac{\Delta T}{e_4}\right)^{e_2}\right)\right] \quad (1)$$

where $E_0 = 29\,900$ ksi (206 GPa) is the value at ambient temperature, $\Delta T$ (in °C) is the increase in temperature above the ambient temperature, and $e_1$ through $e_4$ are coefficients depending on the type of steel. For rolled structural steel, $e_1 = 3.768$, $e_2 = 1.000$, $e_3 = 639$ °C, and $e_4 = 1650$ °C. Fig. 2 shows the degradation of the normalized elastic modulus with increasing temperature using Eq. (1) with the listed coefficients. The temperature-dependence of the yield strength $F_y$ is expressed as:

$$F_y(T) = F_{y0}\left[r_5 + (1-r_5)\cdot\exp\left(-\frac{1}{2}\left(\frac{\Delta T}{r_3}\right)^{r_1} - \frac{1}{2}\left(\frac{\Delta T}{r_4}\right)^{r_2}\right)\right] \quad (2)$$

where $F_{y0}$ is the yield strength at ambient temperature and $r_1$ through $r_5$ are coefficients depending on the type of steel. For rolled structural steel, $r_1 = 7.514$, $r_2 = 1.000$, $r_3 = 588$ °C, $r_4 = 676$ °C, and $r_5 = 0.090$. The degradation of the normalized yield strength with increasing temperature is also shown in Fig. 2 using Eq. (2) with the listed coefficients.

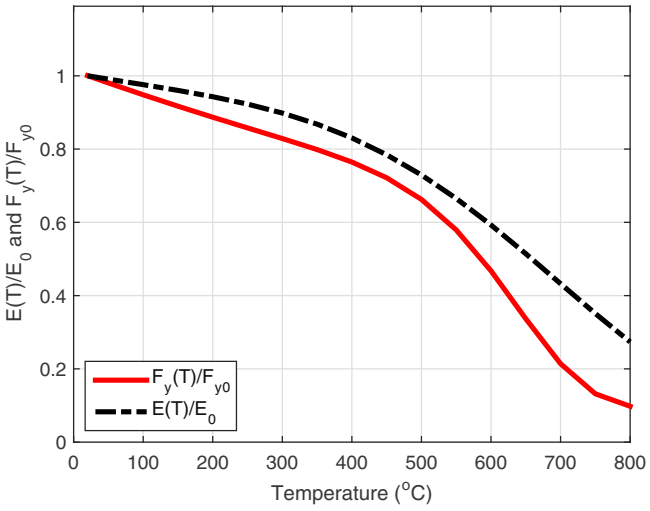


**Fig. 2.** Degradation of normalized yield strength and elastic modulus with temperature for structural steel.

Using the temperature-dependent modulus of elasticity and yield strength, the true stress $\sigma$ is expressed as a function of true strain $\varepsilon$ as follows:

$$\sigma = \begin{cases} E(T)\varepsilon, & \varepsilon < \varepsilon_y(T) \\ \left[F_y(T) + (k_3 - k_4 F_{y0}) \exp\left(-\left(\frac{T}{k_2}\right)^{k_1}\right)(\varepsilon - \varepsilon_y(T))^n\right], & \varepsilon \geq \varepsilon_y(T) \end{cases} \quad (3)$$

where $T$ is temperature (in °C), $\varepsilon_y(T) = F_y(T)/E(T)$ is the temperature-dependent yield strain, $n = 0.503$ is the strain hardening exponent, and the coefficients $k_1$ through $k_4$ have the following values: $k_1 = 7.820$, $k_2 = 540$ °C, $k_3 = 1006$ MPa (145.9 ksi), and $k_4 = 0.759$.

Up to the onset of necking, true stress and strain are related to engineering stress $s$ and engineering strain $e$ by the following equations, based on the assumptions of constant volume and uniform strain along the gauge length of a tensile coupon (e.g., Dieter [10]):

$$\varepsilon = \ln(e+1) \quad (4)$$

$$\sigma = s(e+1) \quad (5)$$

### 2.2. Onset of necking at the ultimate tensile strength

The onset of necking in a tensile coupon occurs at the ultimate tensile strength, when the increase in stress due to reduction of the cross-sectional area overcomes the increase in strength due to strain hardening. At this point the strain, which had been uniform within the gauge length, begins to localize. An equation for the engineering strain at the onset of necking (i.e., the uniform strain), was determined based on nonlinear least-squares regression of data available in the literature (Fig. 3(a)) as:

$$e_u(T) = e_{u0}\left[\exp\left(-\frac{1}{2}\left(\frac{\Delta T}{q_3}\right)^{q_1}\right)\right] \quad (6)$$

where $e_{u0}$ is the uniform strain at ambient temperature, $q_1 = 3.587$, and $q_3 = 488$ °C. The data included in Fig. 3 correspond to a subset of the data considered by Seif et al. [7], for which uniform strain values were reported. The ambient-temperature uniform strain decreases with increasing yield strength (i.e., low-strength steels are typically more ductile than high-strength steels), as shown by the experimental data in Fig. 3(b), and the following approximate relationship was obtained from linear regression of these data:

$$e_{u0}(F_{y0}) = p_1 F_{y0} + p_2 \quad (7)$$

where $p_1 = -0.00152$ and $p_2 = 0.252$. Together, Eqs. (6) and (7) provide a complete description of the temperature-dependent uniform strain, based solely on the ambient temperature yield strength, that can be applied to arbitrary strength steels. Although the stress–strain model is limited to steels with nominal yield strengths less than 65 ksi (450 MPa), the relationship in Eq. (7) was fit to data over a wider range of nominal yield strengths with a maximum nominal yield strength of 110 ksi (760 MPa). The ultimate tensile strength corresponding to a given value of $e_u$ can be calculated using Eqs. (3), (4), and (5). Fig. 4 compares ultimate tensile strength values obtained from the proposed uniform strain model (Eq. (6)) for $F_{y0} = 50$ ksi (345 MPa) with corresponding experimental tensile strength data.

### 2.3. Modeling of post-ultimate-strength necking and fracture

The true stress–strain relationship in Eq. (3) was calibrated based on the available tensile coupon data up to the ultimate tensile strength, which corresponds to the uniform strain $e_u$ given by Eq. (6). In finite element modeling of tensile coupons, direct application of Eq. (3) for strains exceeding $e_u$ was found to result in delayed onset of necking in

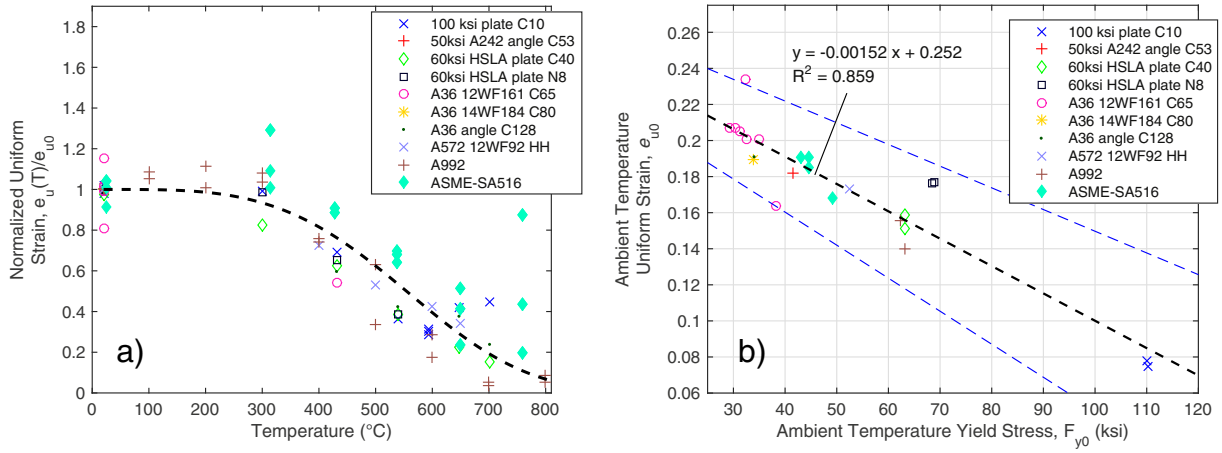


**Fig. 3.** (a) Temperature dependent normalized uniform strain (Eq. (6)) compared with available experimental data and (b) fit to ambient temperature uniform strain based on ambient temperature yield stress with 95% confidence bounds, compared with available experimental data.

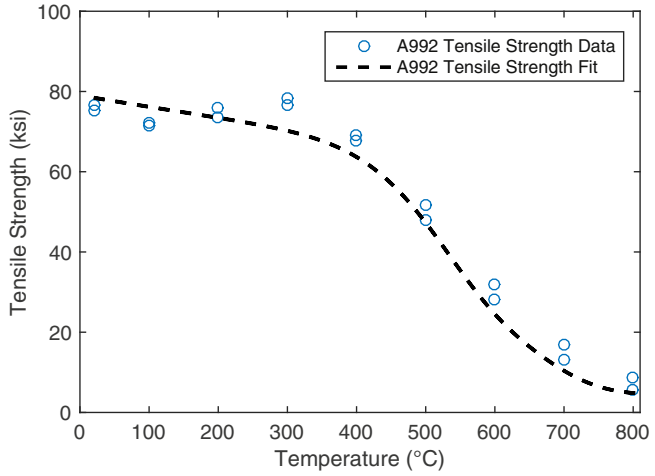


**Fig. 4.** Tensile strength resulting from fit to uniform strain for structural steel with $F_y$ = 50 ksi (345 MPa), compared with experimental data (1 ksi = 6.895 MPa).

comparison with the experimental data. This is illustrated in Fig. 5, in which Fig. 5(a) shows the true stress–strain curve at 400 °C from Eq. (3) (for $F_{y0}$ = 50 ksi (345 MPa)) and Fig. 5(b) shows the corresponding engineering stress–strain curve generated from finite-element analysis of a tensile coupon, using the approach discussed subsequently. The onset of necking corresponds to the Considère criterion for instability in tension (e.g., Dieter [10]), in which the true stress is equal to the slope of the true stress–strain curve, $\sigma = d\sigma/d\varepsilon$. In Fig. 5(a), this point corresponds to the intersection of the solid curve, representing $\sigma(\varepsilon)$ from Eq. (3), with the dashed curve, representing $d\sigma/d\varepsilon$. This intersection occurs at a true strain of $\varepsilon = 0.293$, which corresponds to an engineering strain of $e = 0.340$ according to Eq. (4). From Eqs. (6) and (7), based on experimental data, the expected uniform strain at 400 °C for $F_{y0}$ = 50 ksi (345 MPa) is $e_u = 0.150$. Direct application of Eq. (3) for strains exceeding $e_u$ thus results in onset of necking at a uniform strain approximately twice as large as the expected experimental value.

To overcome this problem, the approach used in this study was to specify the true stress–strain relationship using Eq. (3) only up to the uniform strain defined by Eq. (6). At this point, necking was imposed by reducing the slope of the true stress–strain curve to equal the true stress, thus satisfying the Considère criterion, and projecting the true stress–strain curve linearly thereafter, as follows:

$$\left.\frac{d\sigma}{d\varepsilon}\right|_{\varepsilon>\varepsilon_u} = \sigma(\varepsilon_u) \tag{8}$$

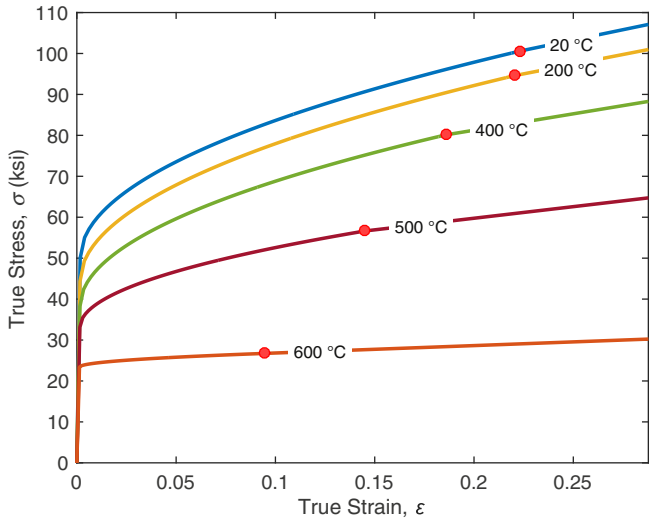


**Fig. 6.** True stress–strain curves for A572 steel, generated using Eq. (3) until the onset of necking (red circular marker) with linearly projected stiffness thereafter (1 ksi = 6.895 MPa). (For interpretation of the references to color in this figure legend, the reader is referred to the web version of this article.)

where $\varepsilon_u = \ln(e_u + 1)$ according to Eq. (4). Fig. 6 shows true stress–strain curves for ASTM A572 Grade 50 steel [11] at various temperatures, generated using this approach. The point corresponding to the onset of necking for each temperature is indicated by a red circle. Fig. 6 shows that at 600 °C, necking initiates at relatively small strain of $\varepsilon_u$ = 6.7%, so that the post-ultimate necking phase constitutes a greater portion of the material response.

In the proposed modeling approach, the failure criterion for element erosion is based on the effective plastic strain, a scalar measure of plastic strain that incorporates its various tensor components. Element erosion is activated when the effective plastic strain in any element (i.e., the local plastic strain in a section or component) exceeds a specified critical value, called the erosion strain $\varepsilon_{er}$. The erosion strain depends on the temperature and on the element discretization in the region of fracture, as is discussed subsequently. As described in the following section, finite element analyses of tensile coupons were performed to calibrate the erosion strain values against available experimental data on elongation of tensile coupons at fracture.

### 2.4. Assumptions and limitations

Although the true stress–strain relationship shown in Eq. (3) is generic and could, at least in principle, be applied to a variety of steels at elevated temperatures, the model was developed based on the

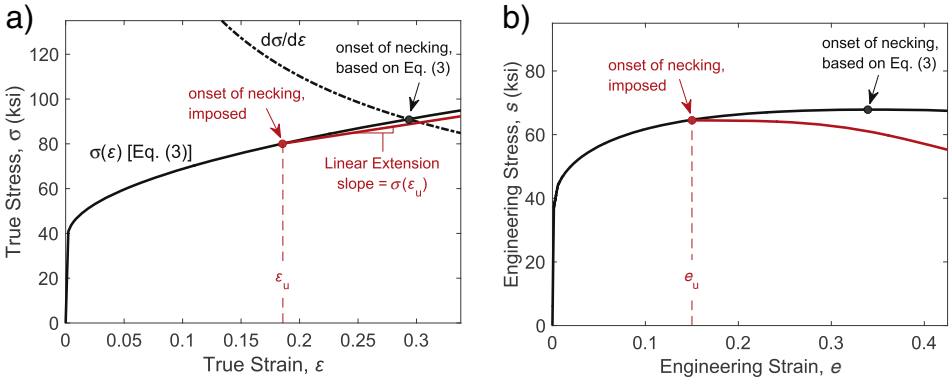


**Fig. 5.** (a) True stress–strain and (b) engineering stress–strain curves comparing the onset of necking resulting from Eq. (3) with that imposed based on experimental data for $e_u$ (400 °C; Fy0 = 50 ksi (345 MPa)).

behavior of structural steels with nominal yield strengths less than 65 ksi (450 MPa) and for temperatures between 20 °C and 800 °C. Application of the model outside of these ranges is not recommended.

For strains exceeding the temperature-dependent uniform strain (Eq. (6)), linear projection of the true stress–strain curves, based on the Considère criterion, successfully initiated necking for all mesh sizes considered. However, it is well known that softening behavior in continuum finite element analyses introduces first-order mesh dependence, and thus the values of erosion strain, which were calibrated against the available tensile test data (see Section 3.3), are mesh-size-dependent. In addition, the erosion strains were calibrated to material within the gauge length of tensile coupons (at elevated temperatures) at their instantaneous triaxiality at fracture. For cases in which the material triaxiality at fracture may differ significantly from that of a tension test, the erosion strain may need to be modified accordingly.

Despite these limitations, this work provides a rational approach to incorporating modeling of fracture in structural steels at elevated temperatures with currently available FE software and tensile coupon data. There does not currently exist sufficient data to support a more sophisticated approach that includes the effects of triaxiality at elevated temperatures.

## 3. Analysis of structural steel tensile coupons

Temperature-dependent values of erosion strain for structural steel members were calibrated against fracture strain values from elevated-temperature coupon tests reported by Luecke et al. [12] and Hu et al. [13]. Using finite-element models of tensile coupons, the erosion strain values were calibrated so that the computed engineering strain at fracture for each temperature matched the average experimental value. Since the simulation of post-ultimate necking and fracture can depend on the mesh discretization, the mesh size used in the calibration procedure needs to be consistent with the mesh size to be used in modeling fracture of a structural component. The influence of mesh size on the computed results is further discussed in Section 3.3.

### 3.1. Tensile test data

Luecke et al. [12] tested a set of A572 Grade 50 steel tensile coupons at elevated temperatures, and four of these test specimens are shown in Fig. 7(a) to illustrate the effect of elevated temperature on the shape and size of the necking region. The thickness of the coupons was 0.125 in (3.175 mm), and the reduced section (where necking and fracture occurred) had a length of $A_o = 1.25$ in (31.75 mm) and a width of 0.24 in (6 mm). The extensometer used in the tests had a gauge length of 0.5 in (12.7 mm). The coupons were first heated to the desired temperature, and then subjected to displacement-controlled tensile loading until fracture. Fig. 7(b) shows engineering stress–strain curves corresponding to the tensile coupons shown in Fig. 7(a). The initial portions of the curves, up to the ultimate tensile strength (plotted with solid lines), correspond to the strain measured by the extensometer. The post-ultimate portions of the curves (plotted with dashed lines) do not represent measured data but are simply straight-line segments connecting the point of necking initiation (at the ultimate tensile strength) to the point of fracture, as explained in the next paragraph.

For consistency with the experiments of Hu et al. [13], discussed subsequently, the engineering strain values at fracture in Fig. 7(b) correspond to a gauge length of $G_o = 1$ in (25.4 mm). This gauge length included 80% of the reduced section and was sufficient to capture the necked region for all specimens. Fracture strain measurements for the 1 in (25.4 mm) gauge length were obtained by using the measured displacement of the actuator in conjunction with the extensometer measurements. The uniform strain at the onset of necking was first obtained from the extensometer measurements. The strain increment from the onset of necking to the time of fracture was then computed by dividing the measured actuator displacement over this time interval by the 1 in (25.4 mm) gauge length. Finally, the computed strain increment was added to the uniform strain at the onset of necking to obtain the total engineering strain at fracture. While elastic rebound of the tensile coupon outside of the necking region was not included in this approach, the associated strains are negligibly small relative to the measured strains at fracture. The resulting values of engineering strain at fracture are plotted at the failure point in Fig. 7(b) and are also plotted as a function of temperature in Fig. 8, along with data from Hu et al. [13].

Hu et al. [13] reported coupon test data for ASTM A992 steel [14] at elevated temperatures, presenting values of engineering strain at fracture for two specimens at each temperature with a gauge length of 1 in (25.4 mm). The data from both Luecke et al. [12] and Hu et al. [13] in Fig. 8 show a similar trend, with the fracture strain initially decreasing with temperature, reaching a minimum value at 400 °C or 500 °C, and then increasing with temperature above 500 °C. The fracture strain values for ASTM A992 steel from Hu et al. [13] are generally somewhat higher than the values for ASTM A572 Grade 50 steel from Luecke et al. [12]. Average values of all the experimental data at 20 °C, 400 °C, 500 °C, and 600 °C are plotted in Fig. 8, connected by a dashed line. These average values were selected as representative failure strain values for structural steel and were used as target values in

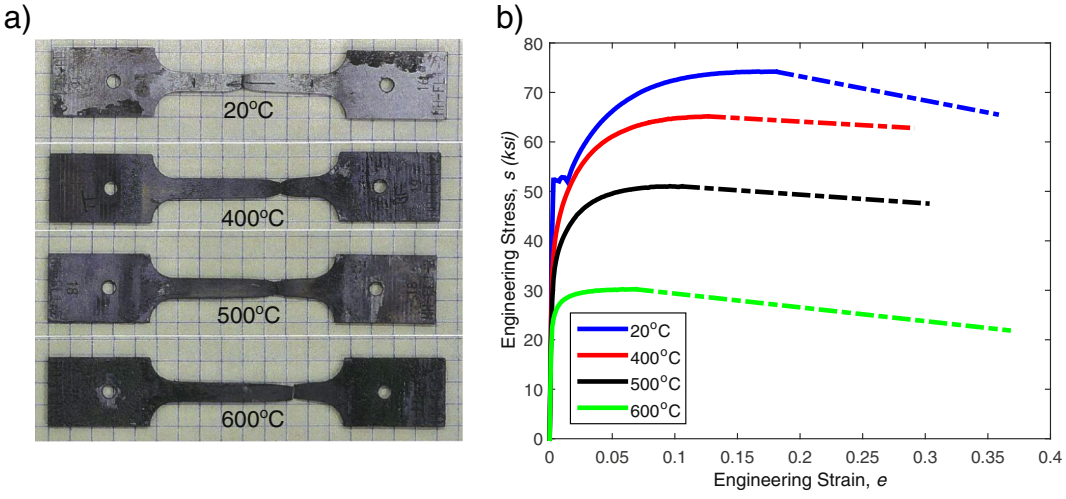


**Fig. 7.** Experimental coupons; (a) picture of the four specimens after the tensile test was conducted at 20 °C, 400 °C, 500 °C, and 600 °C, and (b) corresponding stress–strain curves* (1 ksi = 6.895 MPa). *Estimated coefficient of variation in measured data is 4%.

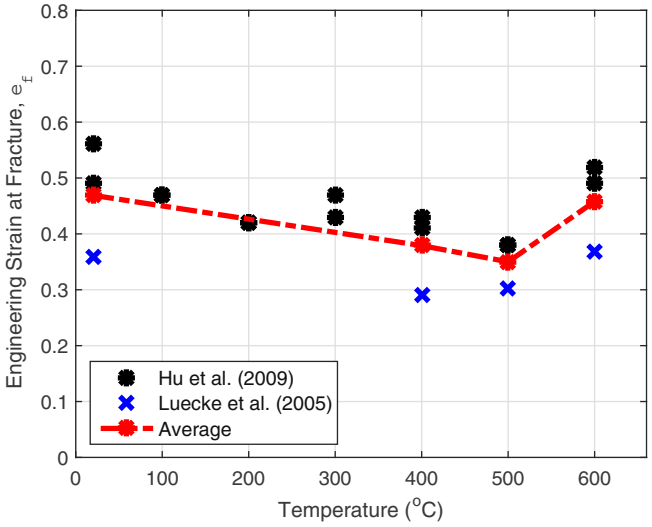


**Fig. 8.** Experimental values of engineering strain at fracture for structural steel*. (Gauge length: 1 in = 25.4 mm). *Estimated coefficient of variation in measured data is 4%.

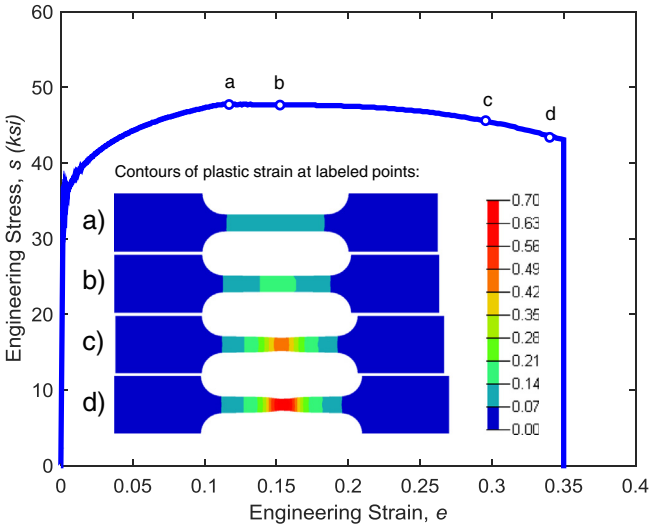


**Fig. 10.** FE analysis results for a tensile coupon model at 500 °C (1 ksi = 6.895 MPa).

calibration of temperature-dependent erosion strain values, as described subsequently.

### 3.2. Finite element modeling approach

The tensile coupons were modeled using three-dimensional solid elements, as illustrated in Fig. 9. Fully integrated eight node elements were used with a typical element size of 0.06 in (1.5 mm). Thus, the reduced section was meshed with four elements across the width and two elements through the thickness. Analyses were performed at uniform temperatures of 20 °C, 400 °C, 500 °C, and 600 °C. As with all subsequent FE analysis reported in this study, the analyses were performed using explicit time integration in LS-DYNA [15], and a smooth functional form of tensile displacement vs. time was used to ensure that dynamic effects were negligible (i.e., to ensure quasi-static loading conditions). The coupons were subjected to tensile loading in the analysis until fracture across the reduced section occurred through element erosion. Element erosion in the necking zone initiated when the effective plastic strain in any element reached the specified erosion strain $\varepsilon_{er}$, at which point that element was removed from the analysis, leading rapidly to erosion of successive elements across the reduced section.

Fig. 10 shows analysis results from uniaxial extension of a tensile coupon at 500 °C. Engineering strain values in the stress–strain curve of Fig. 10 were calculated based on the relative displacement of two nodes at each end of the gauge section, with an initial length of $G_o$ = 1 in (25 mm). Contours of effective plastic strain are also shown in Fig. 10 at different points labeled along the computed stress–strain curve. Point *a* is around the onset of necking (at the ultimate tensile strength) and point *b* is shortly after. The corresponding plastic strain contours show fairly uniform plastic strain values along the gauge length that are comparable to the corresponding engineering strain values. For example, point *b* corresponds to an engineering strain of 0.15, and comparable plastic strains of about 0.14 are observed. However, points *c* and *d* are way after the onset of necking, and the contours of plastic strain indicate localization of strain near the center of the gauge length, with plastic strain values exceeding the corresponding engineering strain. For example, point *d* (just prior to fracture) corresponds to an engineering strain of 0.35, but larger plastic strains of about 0.70 are observed in the necking region. Because of this localization of plastic strain that occurs during necking, erosion strain values are generally larger than the engineering strain values at which fracture occurs. An erosion strain of $\varepsilon_{er}$ = 0.80 was used for the analysis in Fig. 10 to achieve fracture at an engineering strain of 0.35. The following section discusses determination of temperature-dependent erosion strain values for structural steel.

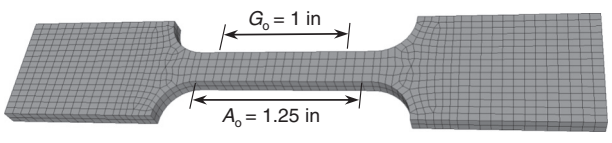


**Fig. 9.** Finite element mesh of a tensile coupon (1 in = 25.4 mm).

### 3.3. Calibration of temperature-dependent erosion strain

Fig. 11 shows the influence of the erosion strain $\varepsilon_{er}$ (the local plastic strain at fracture) on the corresponding engineering strain at fracture obtained from the finite element model of a tensile coupon at 400 °C. As the value of $\varepsilon_{er}$ increases, the engineering strain at fracture also increases. For instance, when $\varepsilon_{er,}$ increases from 0.55 to 0.8, the engineering strain at fracture, $e_f$, increases by about 19% from 0.32 to 0.38. Larger values of the erosion strain produce a longer descending branch of the engineering stress–strain curve, which is associated with

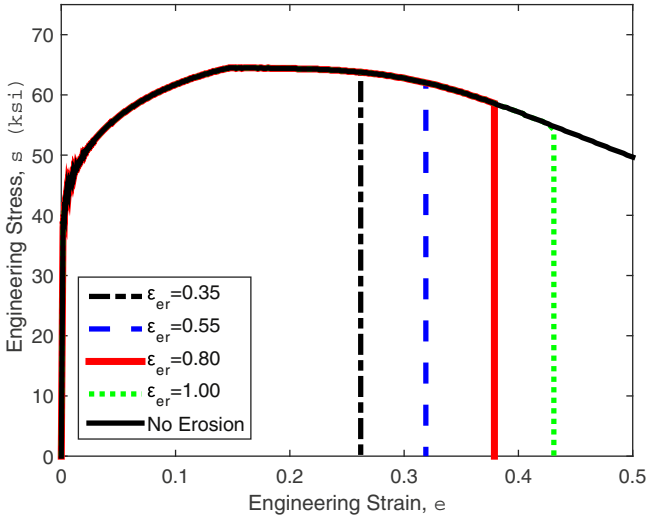


**Fig. 11.** Influence of the erosion strain εer on the computed engineering strain at fracture at 400 °C (1 ksi = 6.895 MPa).

more extensive necking. To determine the appropriate value of erosion strain at each temperature, the erosion strain was adjusted until the resulting engineering strain at fracture matched the target value, which is the average of the experimental data shown in Fig. 8.

Fig. 12 shows the values of erosion strain $\varepsilon_{er}$ used in the FE analyses to obtain the target values of engineering strain at fracture shown in Fig. 8. For all cases, the erosion strain is significantly greater than the engineering strain at fracture (1.63 vs. 0.46, respectively, at 600 °C), indicating extensive necking and associated localization of plastic strains in the post-ultimate phase prior to fracture. When high values of erosion strain are required in a material model, care must be taken to extend the stress–strain curves to the specified erosion strain. Defining stress–strain curves only up to the engineering strain at fracture would require the software to extrapolate stress–strain curves, possibly yielding unreliable results.

Fig. 13 shows engineering stress–strain curves obtained from FE analysis of tensile coupons with the erosion strain values shown in Fig. 12 at temperatures of 20 °C, 400 °C, 500 °C, and 600 °C. As a consequence of the calibration procedure described above, the engineering strain values at fracture in Fig. 13 match the target values in Fig. 8. Note that the stress–strain curves in Fig. 13 should not be expected to closely match the experimental stress–strain curves in Fig. 7(b) for the following reasons:

- The stress–strain curves in Fig. 13 are based on the power–law model in Eq. (3), which was fit to a large set of experimental data, whereas the stress–strain curves in Fig. 7(b) were obtained from individual coupon tests.
- The fracture strain values in Fig. 13 were calibrated to match the average experimental values in Fig. 8, whereas the fracture strain values in Fig. 7(b) were obtained from individual coupon tests.

In spite of these differences, some general similarities can be observed between the computed and experimental curves, including the reduction in the ultimate tensile strength with increasing temperature, the reduced fracture strain at 400 °C and 500 °C, and the early onset of necking and extensive post-ultimate portion of the stress–strain curves at 600 °C. These similarities confirm that the proposed modeling approach captures key aspects of the material behavior at elevated temperatures.

The appropriate values of erosion strain depend on the mesh discretization. The erosion strain values in Fig. 12 were calibrated for coupon models with a typical element size of 0.06 in (1.5 mm) (see Fig. 9). Using a different mesh refinement would require recalibration of the erosion strain values in order to achieve the same engineering strains at failure. Table 1 shows calibrated erosion strain values for the original mesh and for a refined mesh with a typical element size of 0.03 in (0.75 mm), along with the target engineering strain values at fracture used in the calibration. These results show that reducing the element size by one-half requires using erosion strains that are 41% to 46% higher for temperatures up to 500 °C and 33% higher for 600 °C. Fig. 14 shows engineering stress–strain curves computed from finite-element models of a tensile coupon for both the original mesh and the refined mesh. These results demonstrate that the proposed calibration procedure allows consistent values of engineering strain at failure to be achieved using the two levels of mesh refinement. Fig. 14 also includes markers to indicate the premature fracture that occurs if erosion strain values are not recalibrated for the refined mesh. Only the post-ultimate behavior depends on the mesh discretization, because of the softening and strain localization that occur during necking. Larger erosion strain values are required for the refined mesh because of the greater localization that occurs, which also results in somewhat reduced values of engineering stress at fracture, as evident in Fig. 14. The results in Fig. 14 and Table 1 demonstrate the importance of using the same element size in the calibration procedure as will be used in modeling the parts of the structural components at which fracture is expected. A fracture-energy based approach could potentially be used to account for this dependence on element size, and such an approach is being explored in ongoing research.

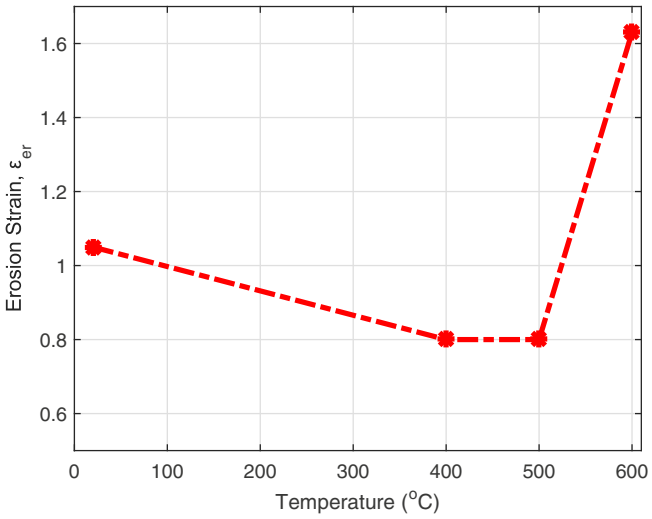


**Fig. 12.** Calibrated values of erosion strain versus temperature for structural steel.

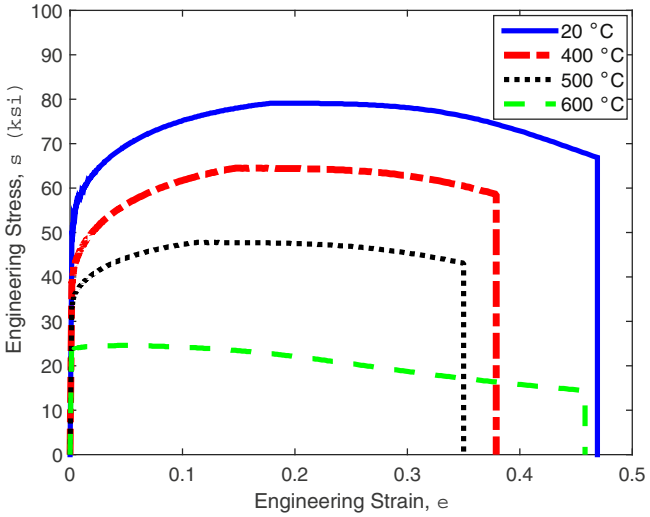


**Fig. 13.** FEA engineering stress–strain curves for selected temperatures with calibrated erosion strain values for structural steel (1 ksi = 6.895 MPa).

## 4. Temperature-dependent material model for structural bolts

Insufficient data were available on structural bolt material properties at elevated temperatures to develop a power–law stress–strain model, as was presented in Eq. (3) for structural steel. Rather,

**Table 1**
Engineering strain values at fracture and corresponding erosion strain values for structural steel.

| Temperature (°C) | Engineering strain at fracture | Erosion strain | |
|---|---|---|---|
| | | Element size: 0.06 in | Element size: 0.03 in |
| 20 | 0.47 | 1.05 | 1.53 |
| 400 | 0.38 | 0.80 | 1.14 |
| 500 | 0.35 | 0.80 | 1.13 |
| 600 | 0.46 | 1.63 | 2.16 |

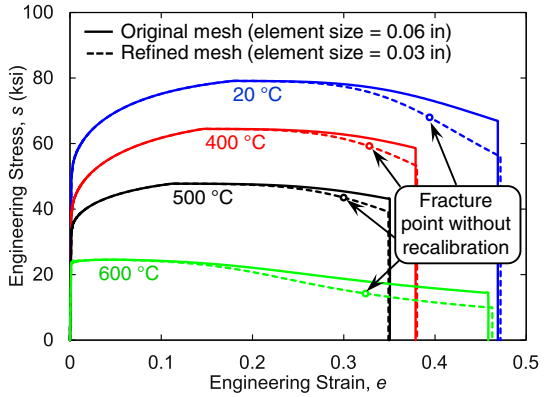


**Fig. 14.** Engineering stress–strain curves computed from finite-element models of a tensile coupon with different levels of mesh refinement (1 ksi = 6.895 MPa; 1 in = 25.4 mm).

a simplified tri-linear representation of the temperature-dependent true stress–strain behavior is proposed in this study, as follows:

$$\sigma = \begin{cases} E(T)\varepsilon, & \varepsilon \le \varepsilon_y(T) \\ F_y(T) + \left[F_u(T) - F_y(T)\right]\dfrac{\varepsilon - \varepsilon_y(T)}{\varepsilon_u(T) - \varepsilon_y(T)}, & \varepsilon_y(T) < \varepsilon \le \varepsilon_u(T) \\ F_u(T) + 0.0008E(T)[\varepsilon - \varepsilon_u(T)], & \varepsilon_u(T) < \varepsilon \end{cases} \quad (9)$$

where $\varepsilon_y(T) = F_y(T)/E(T)$ is the temperature-dependent yield strain. The elastic modulus $E$ is the same for bolts as for structural steel and is calculated from Eq. (1).

For A325 and A490 high-strength bolts, the temperature-dependence of the yield strength $F_y$ is calculated from Eq. (2), with $r_1 = 4.967$, $r_2 = 1.000$, $r_3 = 456$ °C, $r_4 = 2040$ °C, and $r_5 = 0.000$ (Seif et al. [7]). Compared to rolled steel, bolts sustain their $F_y$ value with the increase of temperature until about 400 °C, after which it reduces dramatically relative to structural steel. Fig. 15 shows the degradation of the normalized yield strength with increasing temperature for ASTM A572 rolled steel and ASTM A325 and A490 bolts ([16,17]). Note that at 400 °C, both rolled steel and bolts sustain about 80% of their yield capacity. At 600 °C, rolled steel sustains about 50% of its yield capacity, while bolts sustain about 20% of their yield capacity. The ultimate tensile strength $F_u$ is calculated using Eq. (2) with the same values of $r_1$ through $r_5$ as for the yield strength, but with the ambient-temperature yield strength $F_{y0}$ replaced by the ambient-temperature ultimate strength $F_{u0}$. The temperature-dependent uniform strain, $\varepsilon_u(T)$, is assumed to have a value of 0.1 at 20 °C and to decrease linearly with temperature to a value of 0.05 at 600 °C, as summarized in Eq. (10).

$$\varepsilon_u(T) = \begin{cases} 0.1, & T \le 20^\circ\text{C} \\ 0.1 - 0.05\left(\dfrac{T - 20^\circ\text{C}}{580^\circ\text{C}}\right), & 20^\circ\text{C} < T \le 600^\circ\text{C} \\ 0.05, & T > 600^\circ\text{C} \end{cases} \quad (10)$$

Eq. (7) is an approximate linear fit to elevated-temperature uniform strain data reported by Kodur et al. [19] for both A325 and A490 structural bolts. Beyond the uniform strain, the modulus of the true stress–strain relationship in Eq. (9) was taken as 0.08% of the elastic modulus $E(T)$, which was found to produce necking and softening behavior that were reasonably consistent with the experimental results presented by Kodur et al. [19].

Fig. 16 shows the tri-linear stress–strain relationship of the A490 bolts at 20 °C, 400 °C, 500 °C, and 600 °C. Similar to rolled steel, the failure criterion used for element erosion is based on the effective plastic strain. Element erosion is activated when the effective plastic strain in any element reaches $\varepsilon_{er}$. The erosion strain is temperature-dependent and is calibrated against experimental data using finite-element models of A325 and A490 steel bolt coupons, as described in the following section.

## 5. Analysis of structural bolts

Erosion strain values used to model the failure of structural bolts need to be calibrated against experimental data at elevated temperatures. Since the shear behavior of bolts is often of primary concern in connection performance, we considered the possibility of calibrating erosion strain values using bolt shear test data at elevated temperatures from Yu [18]. However, the measured data included deformations of the test plates that imposed shear forces on the bolts, so that the bolt shear deformations could not be isolated from the published results. Therefore, similar to the procedure used for structural steel, erosion strain values for structural bolts were calibrated against tensile test data at elevated temperatures, using bolt coupon test data from Kodur at al. [19] presented in Section 5.1. After using finite element models of bolt coupons (Section 5.2) to calibrate the erosion strain values against the tensile test data (Section 5.3), the behavior of the proposed modeling approach under shear loading is considered (Section 5.4).

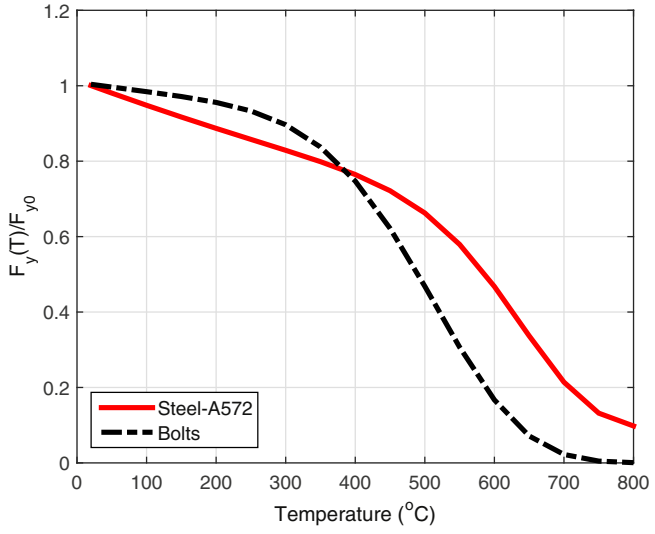


**Fig. 15.** Degradation of normalized yield strength versus the increase in temperature for rolled structural steel and bolts.

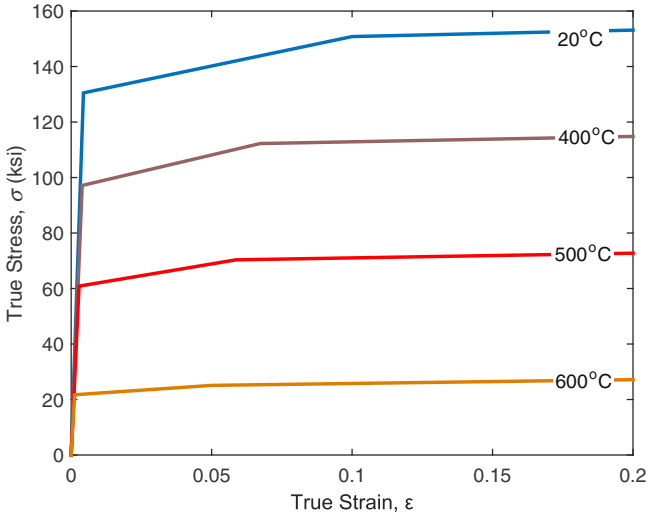


**Fig. 16.** True stress–strain curves for A490 bolts (1 ksi = 6.895 MPa).

### 5.1. Tensile test data

Fig. 17 presents values of engineering strain at fracture for both A325 and A490 bolts reported by Kodur et al. [19] based on tensile tests of bolt coupons at 20 °C, 400 °C, 500 °C, and 600 °C. The reported engineering strain values at fracture correspond to a gauge length of 2 in (50.8 mm). The fracture strain values in Fig. 17 were used as target values in calibration of the erosion strain values, as described subsequently.

### 5.2. Finite element modeling approach

Tensile coupons machined from A325 and A490 bolts were modeled using three-dimensional solid elements, as illustrated in Fig. 18. Fully integrated eight node elements were used with a typical element size of 0.06 in (1.5 mm). Analyses were performed at uniform temperatures of 20 °C, 400 °C, 500 °C, and 600 °C. The bolts were subjected to tensile loading in the analysis until necking and fracture occurred in the reduced section of the bolt coupon. Fracture was modeled through element erosion, which initiated when the effective plastic strain in elements in the necking zone reached the specified erosion strain, $\varepsilon_{er}$.

Fig. 19 shows analysis results from uniaxial extension of an A490 bolt coupon at 500 °C. Engineering strain values were calculated based on the relative displacement of nodes at each end of the gauge section, with an initial length of $G_o = 2$ in (50.8 mm), corresponding to the tests by Kodur et al. [19]. Contours of effective plastic strain are also shown in Fig. 19 for the points labeled on the computed stress–strain curve. Point *a* is at the onset of necking, and the corresponding plastic strain contours show uniform plastic strains of about 0.06 along the gauge length that are comparable to the corresponding engineering strain value of 0.06. However, points *b* and *c* are after the onset of necking, and the contours of plastic strain indicate localization of strain where necking occurs near the center of the reduced section. The plastic strains in the necking zone exceed the corresponding engineering strains. For example, point *c* (just prior to fracture) corresponds to an engineering strain of about 0.16, but much larger plastic strains of about 0.39 are observed in the necking region. The following section discusses determination of temperature-dependent erosion strain values for bolts.

### 5.3. Calibration of temperature-dependent erosion strain

To determine the appropriate value of erosion strain at each temperature, the erosion strain was adjusted until the resulting engineering strain at fracture matched the target value shown in Fig. 17, obtained from the experimental data of Kodur at al. [19]. These target values of engineering strain at fracture are also listed in Table 2 (columns 2 and 3), along with the calibrated values of erosion strain used in the FE models (columns 3 and 4). The calibrated values of erosion strain are plotted against temperature in Fig. 20. Figs. 21 and 22 show engineering stress–strain curves obtained from FE analysis of A325 and A490 bolts, respectively, at temperatures of 20 °C, 400 °C, 500 °C, and 600 °C. The calibration procedure employed ensures that the engineering strain values at fracture precisely match the target values from Kodur et al. [19]. At all temperatures, the A490 bolts are stronger and fracture earlier than the A325 bolts. For both types of bolts, the engineering strain at fracture is fairly constant from ambient temperature up to 400 °C, but increases above 400 °C. Above 400 °C the strength of bolts drops more rapidly than the strength of rolled structural steel, as shown in Fig. 15.

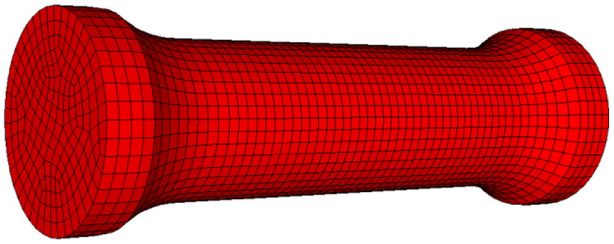

**Fig. 18.** Finite element mesh of a bolt tensile coupon.

### 5.4. Performance in shear

While the material model for structural bolts and the associated erosion strain values were developed and calibrated on the basis of tensile test data, it is important that the modeling approach is also capable of capturing the behavior and failure of structural bolts in shear. To verify the adequacy of the modeling approach in representing shear behavior, FE analyses were performed of a series of double-shear bolt tests. Solid-element models of double-shear test specimens were developed with dimensions corresponding to tests conducted by Wallaert and Fisher [20] at ambient temperature. Material properties for ASTM A36

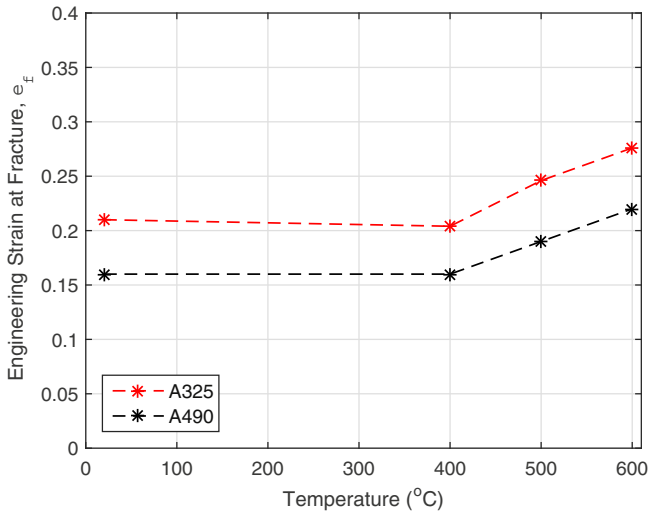


**Fig. 17.** Experimental values of engineering strain at fracture from Kodur et al. (2012) for A325 and A490 bolts.

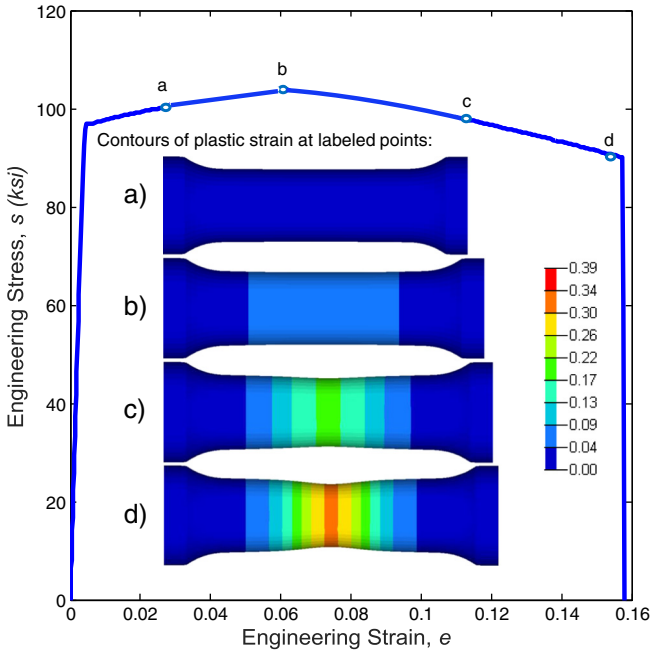


**Fig. 19.** FE analysis results for an A490 bolt tensile coupon at 500 °C (1 ksi = 6.895 MPa).

**Table 2**
Engineering and erosion strain values at fracture for A325 and A490 bolts.

| Temperature (°C) | Engineering strain at fracture | | Erosion strain at fracture[a] | |
|---|---|---|---|---|
| | A325 | A490 | A325 | A490 |
| 20 | 0.21 | 0.16 | 0.50 | 0.35 |
| 400 | 0.20 | 0.16 | 0.55 | 0.40 |
| 500 | 0.25 | 0.19 | 0.75 | 0.55 |
| 600 | 0.28 | 0.22 | 0.75 | 0.60 |

[a] Typical element size of 0.06 in (1.50 mm).

steel [21] were used for modeling the bearing plates, which are comparable to the properties of the steel plates used in the tests. Due to symmetry, only half of each specimen was modeled, with boundary conditions reflecting the symmetry as shown in Fig. 23(a). The center plate was subjected to tensile loading in the analysis, which subjected the bolts to double shear until fracture across the bolt occurred. Fracture initiated when the effective plastic strain in any elements reached the specified erosion strain, $\varepsilon_{er}$, as discussed in previous sections. Fig. 23(b) shows the solid-element mesh of the bolt after shear fracture.

The double-shear analysis results for an A325 bolt at ambient temperature are plotted in Fig. 24 with experimental results from Wallaert and Fisher [20]. Note that these experimental curves are best fit to data from several tests; the estimated coefficient of variation in measurements is 4%. At ambient temperatures, the shear capacity of the A325 bolts was 79 ksi (545 MPa), which is within 1% of the experimental results, and within 5% of the nominal shear capacity of 75 ksi (517 MPa) specified by the Research Council on Structural Connections (RCSC [22]). The FE results simulated the experimental results reasonably well, particularly for the shear stress at fracture. The test specimen sustained somewhat larger deformations than the FE model before fracture, likely due to the deformations of the plates during the experiment. The shear capacity obtained from the FE model for the A490 bolts at ambient temperature was 96 ksi (660 MPa), within 2% of the nominal shear capacity of 94 ksi (646 MPa) specified by RCSC [22]. Note that the nominal shear capacities reported here were obtained by dividing the nominal shear capacity listed in Table 5.1 of the specification [22] by a factor of 0.80 to eliminate the reduction in strength that accounts for non-uniform shear force distribution, since the shear force is carried by a single bolt.

Using the proposed modeling approach for structural bolts, Figs. 25 and 26 show shear stress vs. deformation curves for bolt shear failure from the FE analyses at 20 °C, 400 °C, 500 °C, and 600 °C, for the A325 and A490 bolts, respectively. Fig. 27 shows a comparison of the computed shear strength values for A325 bolts from Fig. 25 with experimental measurements reported by Yu [18] and by Kodur et al. [19], with all results normalized by the ambient-temperature shear strength. While there is scatter in the experimental data in Fig. 27, the computed values are seen to be consistent with the measured data, confirming that the proposed modeling approach can capture the degradation in the shear strength of bolts with increasing temperature.

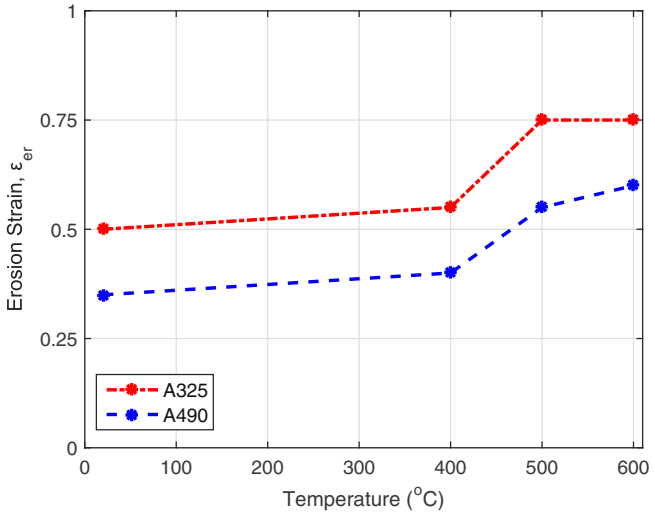


**Fig. 20.** Calibrated values of erosion strain versus temperature for A325 and A490 bolts.

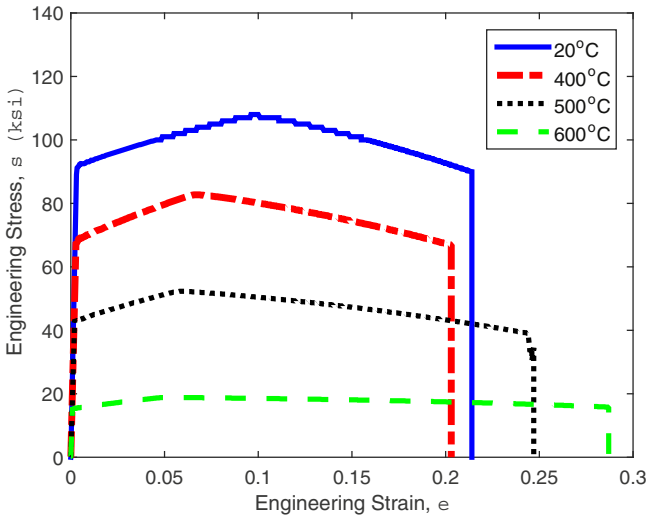


**Fig. 21.** Computed stress–strain curves from an FE model of an A325 bolt coupon at elevated temperatures (1 ksi = 6.895 MPa).

## 6. Summary, conclusions, and future work

A practical modeling approach has been developed to represent temperature-dependent nonlinear behavior and failure of structural steel and structural bolts at elevated temperatures, using element erosion to represent material failure. This modeling approach can be used in explicit finite element analyses to represent the successive failures of components in bolted connections under fire-induced heating and the consequent redistribution of loads. For structural steel materials, a temperature-dependent power–law model was used to represent the true stress–strain behavior up to the onset of necking at

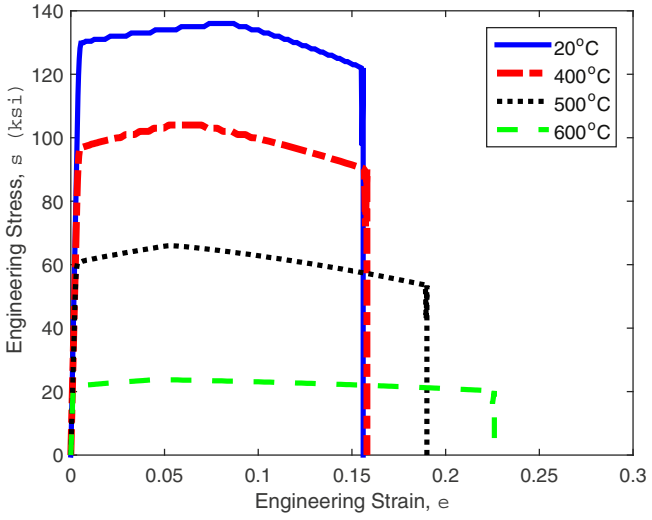


**Fig. 22.** Computed stress–strain curves from and FE model of an A490 bolt coupon at elevated temperatures (1 ksi = 6.895 MPa).

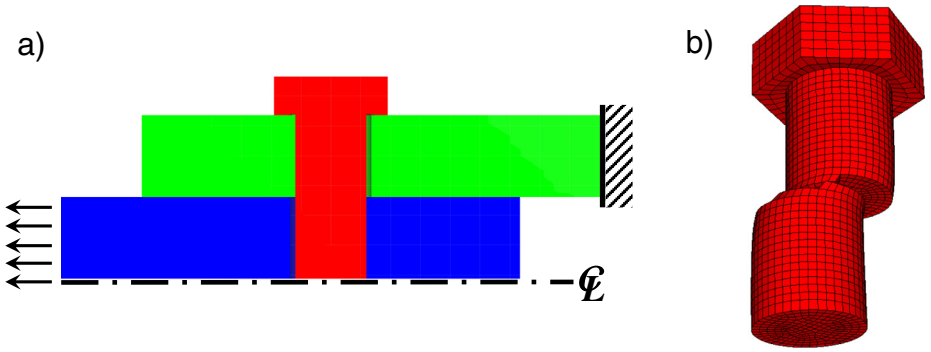


**Fig. 23.** Detailed model of a double-shear bolt test: (a) section view, (b) bolt after fracture.

the temperature-dependent uniform strain. The uniform strain was determined based on a nonlinear least-squares fit to the uniform strain data for elevated temperatures available in the literature. The post-ultimate behavior was represented by a linear projection of the true stress–strain curve, based on the Considère criterion, to initiate necking at the uniform strain. Due to the more limited experimental data on structural bolts at elevated temperatures, a simpler tri-linear material model was proposed to represent the true stress–strain behavior of structural bolts.

A relatively simple plastic strain-based failure criterion was used to activate element erosion, noting that the currently available experimental data on fracture of structural steel and structural bolts at elevated temperatures are insufficient to enable calibration of micromechanics-based models for ductile fracture. Values of erosion strain at elevated temperatures were calibrated against experimental data on the engineering strain at fracture of tensile coupons, using FE models of tensile coupons to determine appropriate values of erosion strain at each temperature. For structural steel, average failure strain values from tensile coupons of ASTM A572 Grade 50 and ASTM A992 steel were used as target values in the calibration of erosion strain. For structural bolts, erosion strain values were calibrated separately for ASTM A325 and A490 bolts, using failure strain data from tensile coupons of each type of bolt.

Because the modeling of post-ultimate softening and strain-localization behavior is known to depend on the mesh discretization, FE analyses of tensile coupons were performed with two levels of mesh refinement, to investigate the sensitivity of the results to mesh size. The results were found to be particularly sensitive to mesh size at high temperatures, because of the earlier onset of necking and the more extensive softening behavior prior to fracture. When the element size was reduced by one-half to 0.03 in (0.75 mm) in an FE analysis of a tensile coupon at 600 °C, with the erosion strain unchanged, the computed engineering strain at fracture was reduced by 44%. The computed results at lower temperatures were less sensitive to the mesh refinement, with their computed engineering strains at fracture reduced by approximately 20%. However, these results confirmed the importance of calibrating erosion strain values using the same mesh size that will be used in analyzing the failure of structural components.

Because the material model and erosion strain values for structural bolts were developed and calibrated to represent tensile behavior, FE analyses of double-shear test specimens were performed to verify that the model was also capable of representing the behavior of structural bolts under shear loading. The computed shear behavior for an A325 bolt compared well with experimental data at ambient temperature: the ultimate shear capacity was within 1% of the experimental value, although the experimental displacement at fracture was somewhat higher than that predicted by the FE analysis, likely due to deformation of the plates during the experiment. Comparing to the nominal shear capacities, the shear capacity computed from the FE analyses at ambient temperature was found to be within 5% for A325 bolts and within 2% for A490 bolts.

The primary conclusions from this research are:

- Analysis of the available experimental data showed that the uniform strain (i.e., the engineering strain at the onset of necking) decreased with increasing temperature.

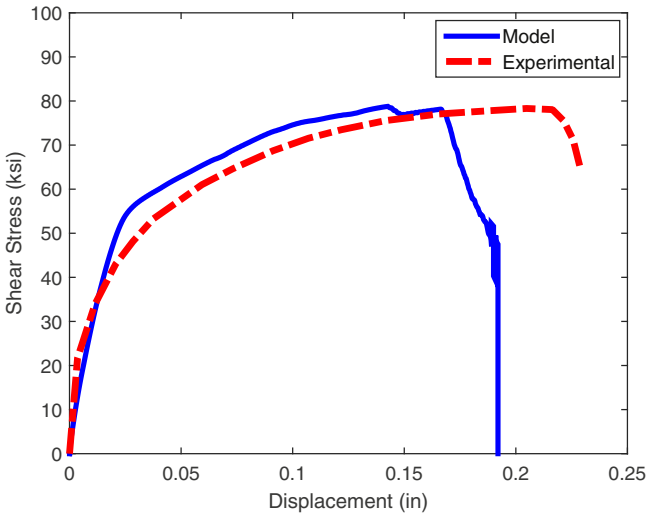


**Fig. 24.** FE model and experimental results (Wallaert and Fisher 1965) for shear displacement of an A325 bolt at ambient temperature (1 ksi = 6.895 MPa).

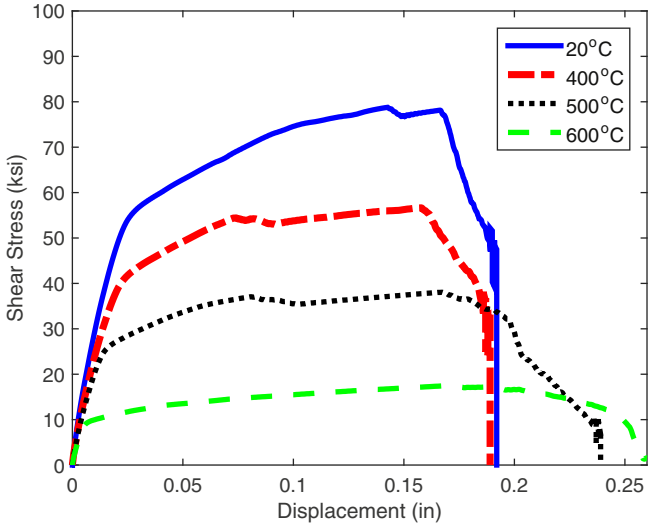


**Fig. 25.** FE results for shear displacement of an A325 bolt at selected temperatures (1 ksi = 6.895 MPa).

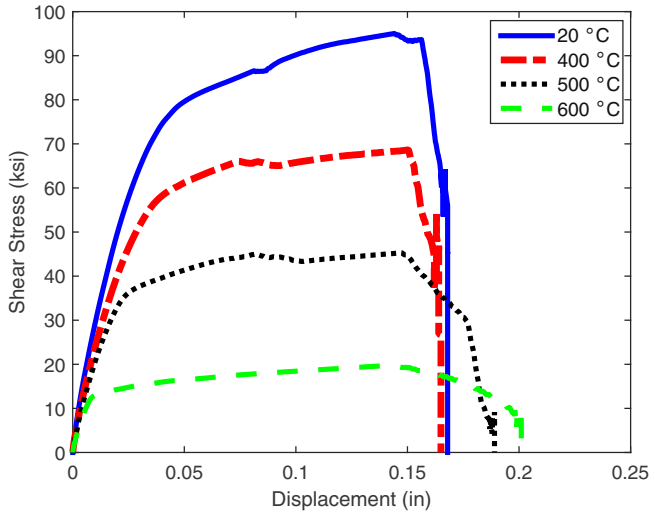


**Fig. 26.** FE results for shear displacement of an A490 bolt at selected temperatures (1 ksi = 6.895 MPa).

- Imposing a reduced stiffness onto the true stress–true strain curve for strains greater than the uniform strain, based on the Considère criterion, was sufficient to initiate necking at the uniform strain at each temperature.
- The fracture strain was dependent on the temperature.

Due to the limitations both in the presented modeling approach and in the currently available experimental data for material behavior and fracture at elevated temperatures, NIST researchers are currently planning future work including carefully controlled experiments with different levels of triaxiality at different temperatures. These tests will be used to explore ductile fracture characteristics at elevated temperatures.

## Disclaimer

Certain commercial software or materials are identified to describe a procedure or concept adequately; such identification is not intended to imply recommendation, endorsement, or implication by the National Institute of Standards and Technology (NIST) that the software or materials are necessarily the best available for the purpose.

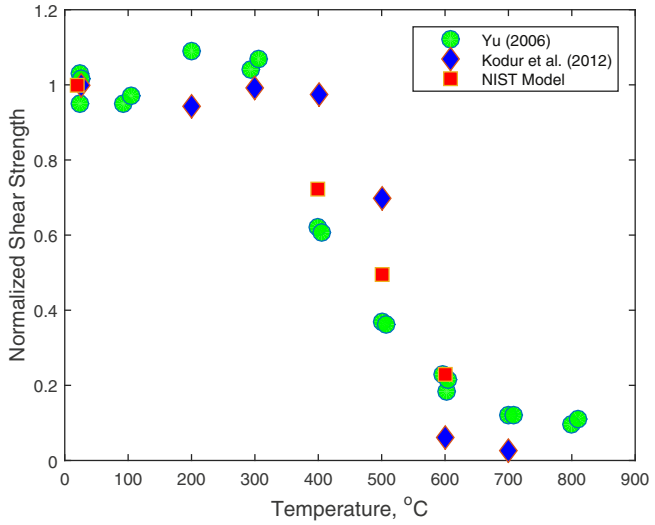


**Fig. 27.** Normalized shear strength versus temperature for A325 bolts.

The Policy of NIST is to use metric units in all its published materials. Because this paper is partially intended for the U.S. steel construction industry which uses in-pound units, it is more practical and less confusing to use in-pound units, in some cases, rather than metric units within quoted text. However, in most cases, units are presented in both metric and in-pound systems.

Another policy of NIST is to include statements of uncertainty with all NIST measurements. In this document, however, some measurements of authors outside of NIST are presented, for which uncertainties were not reported and are unknown.

## References

[1] Seif MS, Main JA, McAllister TP. Performance of steel shear tab connections at elevated temperatures. Proceedings of the annual stability conference. St. Louis, Missouri: Structural Stability Research Council; 2013 [April 16-–20, 2013].
[2] Kanvinde AM, Deierlein GG. Void growth model and stress modified critical strain model to predict ductile fracture in structural steels. J Struct Eng 2006;132(12):1907–18.
[3] Garlock ME, Selamet S. Modeling and behavior of steel plate connections subject to various fire scenarios. J Struct Eng 2010;136(2010):897–906.
[4] Sarraj M, Burgess IW, Davison J, Plank RJ. Finite element modelling of steel fin plate connections in fire. Fire Saf J 2007;42:408–15.
[5] Pakala P, Kodur V, Dwaikat M. Critical factors influencing the fire performance of bolted double angle connections. Eng Struct 2012;42:106–14.
[6] European Committee for Standardization. Eurocode 3: design of steel structures. part 1.2: general rules structural fire design. *ENV 1993-1-2:2001*, Brussels, Belgium; 2001.
[7] Seif M, Choe L, Main JA, Zhang C, Weigand J, Gross J, et al. Temperature-dependent material modeling for structural steels: formulation and application. NIST technical note TN-1907. Gaithersburg, MD: National Institute of Standards and Technology; 2016. http://dx.doi.org/10.6028/NIST.TN.1907.
[8] Sadek F, Main JA, Lew HS, El-Tawil S. Performance of steel moment connections under a column removal scenario. II: Analysis. J Struct Eng 2013;139(1):108–19.
[9] Main JA, Sadek F. Modeling and analysis of single-plate shear connections under column loss. J Struct Eng 2013. http://dx.doi.org/10.1061/(ASCE)ST.1943-541X.0000866.
[10] Dieter GE. Mechanical metallurgy. 2nd ed. New York: McGraw-Hill; 1976.
[11] ASTM International. Standard specification for high-strength low-alloy columbium–vanadium structural steel. *ASTM A572/A572M-13a*, West Conshohocken, PA; 2013. http://dx.doi.org/10.1520/A0572_A0572M.
[12] Luecke WE, McColskey JD, McCowan CN, Banovic SW, Fields RJ, Foecke TJ, et al. Federal Building and fire safety investigation of the World Trade Center disaster, mechanical properties of structural steels. NIST NCSTAR 1-3D. Gaithersburg, MD: National Institute of Standards and Technology; 2005.
[13] Hu G, Morovat MA, Lee J, Schell E, Engelhardt M. Elevated temperature properties of ASTM A992 steel. ASCE- structures congress proceedings,; 2009. p. 1067–76.
[14] ASTM International. Standard specification for structural bolts, alloy steel, heat treated, 150 ksi minimum tensile strength. *ASTM A992/A992M-11*, West Conshohocken, PA; 2012. http://dx.doi.org/10.1520/A0992_A0992M-11.
[15] Livermore Software Technology Corporation (LSTC). *LS-DYNA Keyword User's Manual, Version 971*, Livermore, CA; 2012.
[16] ASTM International. Standard specification for structural bolts, steel, heat treated, 120/105 ksi minimum tensile strength. *ASTM A325-10e1*, West Conshohocken, PA; 2010. http://dx.doi.org/10.1520/A0325.
[17] ASTM International. Standard specification for structural bolts, alloy steel, heat treated, 150 ksi minimum tensile strength. *ASTM A490-12*, West Conshohocken, PA; 2012. http://dx.doi.org/10.1520/A0490-12.
[18] Yu L. Behavior of bolted connection during and after a fire. [Ph.D. dissertation] Austin, TX: Univ. of Texas at Austin; 2006.
[20] Wallaert JJ, Fisher JW. Shear strength of high-strength bolts. J Struct Div ASCE 1965;91(ST3):99–125.
[19] Kodur V, Kand S, Khaliq W. Effect of temperature on thermal and mechanical properties of steel bolts. J Mater Civ Eng 2012;24(6):765–74.
[21] ASTM International. Standard specification for carbon structural steel. *ASTM A36/A36M-12*, West Conshohocken, PA; 2012. http://dx.doi.org/10.1520/A0036_A0036M-12.
[22] Research Council on Structural Connections (RCSC). Specifications for structural joints using ASTM A325 or A490 bolts. Chicago: AISC; 2004.